nature communications

Article

https://doi.org/10.1038/s41467-026-76031-3

Observed thresholds in sea-level rise driving global tidal wetland loss

Received: 29 January 2026

Accepted: 15 July 2026

Published online: 25 July 2026

Check for updates

Jiejun Luo[1,2], Avril Hardi[2], Zhijun Dai[1] ✉, Wiebe Nijland[2], Xuefei Mei[1], Jie Wang[1,3] & Jaap H. Nienhuis[2] ✉

Tidal wetlands, such as salt marshes and mangroves, are highly vulnerable to drowning under accelerating relative sea-level rise. Yet its role as a driver of wetland loss has thus far been difficult to establish. Here we integrate multi-source remote sensing data spanning the past two decades and show that wetland area loss accelerates nonlinearly as relative sea-level rise rates increase. We find a critical threshold of 9 mm yr^{-1}, beyond which the probability of loss acceleration exceeds 92% and the loss rate rises eightfold. Although salt marshes and mangroves share a similar threshold for abrupt loss acceleration, their trajectories diverge before reaching it: salt marshes exhibit modest and progressive area reduction, whereas mangroves remain comparatively stable until the threshold is crossed. Globally, lateral wetland change exhibits a marginally higher threshold than direct inundation loss (~ 8 mm yr^{-1}), suggesting that lateral dynamics, modulated by tidal range and sediment supply, can partially buffer against rapid loss onset. These findings provide an empirical benchmark for refining projections of coastal wetland vulnerability and guiding management interventions.

Tidal wetlands, including salt marshes and mangroves, rank among the most productive ecosystems on the Earth[1,2], and have experienced widespread surface area loss in recent decades[3]. Relative sea-level (RSL) rise, accelerated by global warming[4], is likely a driver of global wetland loss, but its effect remains uncertain[5,6].

The crux of this uncertainty lies in translating vertical, site-specific records of wetland response to RSL rise into surface area change. Many studies have shown clear vertical response to RSL rise across various timescales. Early Holocene (12–8 ka BP) records indicate that rapid RSL rise rates exceeding 8 mm yr^{-1} (ref. 7) are associated with widespread conversion of salt marshes to subtidal facies[6] with similar patterns in mangroves[8]. RSL rise deceleration later in the Holocene, conversely, led to wetland expansion[9–11]. Surface elevation tables and marker horizons (SET-MH) implemented since the 1990s[12–14], show extensive submergence of wetland surfaces relative to RSL rise on the Louisiana coast[15,16] and in the Indo-Pacific region[17]. However, widespread vertical sediment accretion has also been observed, often matching or exceeding rates of RSL rise[13,18]. These contrasting findings stem from a key limitation: point-based sedimentary archives, embedded in local settings, are biased to places that accrete[19], and may not represent broader trends in wetland area[5,12,13]. Indeed, the study of Saintilan et al.[20] investigated lateral wetland change in the proximity to SET-MH stations, and found an increasing probability of contraction as RSL rise accelerates. However, the lack of global investigations implies a fragmented understanding of this issue, with studies reporting divergent response thresholds to RSL rise (see compilation in Table 1).

To circumvent the limitations of local studies, numerical models have been built to complement point-wise records of wetland responses to RSL rise[21–23]. These models indicate a nonlinear vertical adjustment to RSL rise[24–26] with landward expansion sometimes overcompensating for coastal loss[27]. These models also project wetland areal response to RSL changes and modifications to tidal range and sediment availability[4,17,28–32]. Yet due to limited global observations, lateral processes in these models remain poorly constrained, and

[1]State Key Laboratory of Estuarine and Coastal Research, East China Normal University, Shanghai, China. [2]Department of Physical Geography, Utrecht University, Utrecht, The Netherlands. [3]State Key Laboratory of Climate Resilience for Coastal Cities, Department of Civil and Environmental Engineering, The Hong Kong Polytechnic University, Hong Kong, China. ✉e-mail: zjdai@sklec.ecnu.edu.cn; j.h.nienhuis@uu.nl

https://doi.org/10.1038/s41467-026-76031-3

Table 1 | Existing threshold estimates of tidal wetlands in response to sea-level rise

Source	Tidal wetland type	Study area	Material	Definition	Threshold value	Spatial dimension
McKee et al.[24]	Mangroves	Caribbean coast	SET-MH stations & Geological records (22 peats, 1 wood, and 1 shell)	Exceeding which the wetland would not persist	5 mm/yr	Vertical
Kirwan et al.[68]	Salt marshes	USA: Plum Island Estuary; Pamlico Sound; Bayou Chitique; North Inlet Estuary; Phillips Creek Marsh, Old Oyster Bayou; NL: Scheldt Estuary	Numerical conceptual model	Maximum rate conducive to wetland stability	~5 to ~10 mm/yr depending on regional tidal range and SSC	Vertical
Kirwan et al.[27]	Salt marshes	—	Numerical conceptual model	Exceeding which abrupt area (width) loss acceleration occurs *1	8–9 mm/yr	Lateral
Wu et al.[97,98]	Salt marshes	Grand Bay, US	Spatially explicit model	Rate corresponding to the shift in specific landscape metrics for 2100	8.4 mm/yr; 7.29 to 11.12 mm/yr	Lateral
Horton et al.[82]	Salt marshes	54 locations of Great Britain	Geological records (54 locations)	Rate corresponding to specific marsh drowning probability	>90% drowning: 7.1 mm/yr >66% drowning: 4.6 mm/yr	Vertical
Saintilan et al.[11]	Mangroves	78 locations globally: Northern Australia, Pacific Islands, SE Asia, Middle East, South America, Caribbean, Central America, North America	Geological records (122 reconstructions)	Rate corresponding to the specific probability of initiation of mangrove vertical adjustment	>90% initiation: 6.1 mm/yr >66% initiation: 4.3 mm/yr	Vertical
Törnqvist et al.[6]	Salt marshes	Louisiana Coast, US	Geological records (355 boreholes)	Rate corresponding to specific marsh drowning probability *2	>90% drowning: 4.6 mm/yr >66% drowning: 3.1 mm/yr	Vertical
				Exceeding which, marsh conversion into open water occurs in about 50 years	6–9 mm/yr	Lateral
Holmquist et al.[70]	Salt marshes	Contiguous United States	Generated vertical resilience index	Exceeding which marshes fail to accrete relative to RSL rise	6.7 mm/yr	Vertical
Saintilan et al.[14]	Salt marshes	477 locations globally: Australia; South Africa; Bay of Fundy, Canada; UK; Belgium, the Mississippi, USA; the Ebro, Spain; Venice Lagoon; Southern California; the US Gulf of Mexico; US Atlantic and North Pacific coastlines	SET-MH stations (477 stations)	Rate corresponding to specific deficit probability	>90% deficit: 7.6 mm/yr >66% deficit: 3.6 mm/yr	Vertical
Saintilan et al.[20]	Mangroves	190 locations globally: Florida,USA; Louisiana, USA; Belize; Victoria, Australia; NSW, Australia; Queensland, Australia; Western Australia; Northern Territory; Micronesia; New Zealand	SET-MH stations (190 stations)	Rate corresponding to specific deficit probability	>90% deficit: 7.9 mm/yr >66% deficit: 4.3 mm/yr	Vertical
	Salt marshes	Vicinity of the mentioned SET-MH stations	Remote sensing products (tidal wetland area change)	Rate corresponding to specific contraction probability	>50% contraction: 5.4 mm/yr *3	Lateral
	Salt marshes	Vicinity of the mentioned SET-MH stations	Remote sensing products (change in surface water occurrence)	Rate corresponding to a specific probability for water cover conversion	>66% conversion: 2.3 mm/yr *4	Lateral
Li et al. (ref. 16)	Salt marshes	Louisiana Coast, US	SET-MH stations (253 stations)	Rate corresponding to a specific deficit probability	>75% deficit: 6.8 mm/yr	Vertical
This study	Salt marshes and mangroves	Global coverage (0.25° grid-cell scale)	Remote sensing products (net area change)	At which abrupt area loss acceleration occurs	9 mm/yr	Lateral
			Remote sensing products (area loss to open water)		8 mm/yr	

Studies are ordered chronologically by publication year, from earliest to most recent.

*1 This threshold is identified from literature results by this study, not stated as conclusions in the original studies.

*2 Original data are from ref. 6 and recalculated using a unified approach by Saintilan et al.[21].

*3 No probability exceeding 66% were found.

*4 No probability exceeding 90% were found.

validation of projected responses is still lacking[4,20,33]. Hence, global observations of wetland lateral change in response to RSL change are critically needed to better understand their future.

In this study, we assess the relationship between tidal wetland area change and RSL change over the past two decades using globally available spatial datasets. We compare global wetland area changes compiled from four newly released datasets (two for salt marshes[3,34] and two for mangroves[3,35]) with local RSL changes at 0.25° grid resolution. The RSL change map is constructed by combining geocentric sea level change[36] and vertical land motion (VLM; ref. 37) for the same period. To enable comparison across grids, we normalize area change rates against the global salt marsh and mangrove extent (see Methods), which defines the relative rate of area change (RRAC). For example, an RRAC of +1% yr^{-1} indicates a yearly wetland gain in a cell corresponding to 1% of the cell's total wetland extent in the reference year of observation. To explore overall lateral dynamics and inundation-related loss in tidal wetlands, we calculate the relative rate of net area change (still referred to as RRAC hereafter) and, separately, the relative rate of area converted to open water (hereafter RROW). To balance data coverage with the inclusion of sufficient wetland area per grid for reliable RRAC calculation, a cutoff of 1 km^2 per grid cell is applied (see Methods). This results in 7264 valid grid cells for tidal wetlands (Supplementary Table 1). By analyzing the relationship between RRAC values and RSL change rates, and explicitly accounting for uncertainties, we aim to address three key questions: (1) how do tidal wetlands respond laterally to rising RSL at the global scale; (2) are changes to rising RSL gradual or thresholded; and (3) do salt marshes and mangroves respond differently? We also examine the roles of two key natural factors frequently highlighted in previous studies—tidal range and suspended sediment concentration (SSC)—in shaping these responses.

Results

Global map of relative sea-level and wetland area change

Our global synthesis reveals a generally negative relationship between RRAC and RSL change in both spatial and frequency distributions. Latitudinally, RSL change and RRAC exhibit approximately symmetric patterns about the zero line, with RSL change rate decreasing and RRAC increasing from lower to higher latitudes (Fig. 1a). This mirror-image pattern is also reflected in some local peaks and troughs of both components (Fig. 1a).

In terms of frequency, net loss occurs more commonly under rising RSL than under falling RSL: 60.2% of tidal wetland grid cells experience net loss under RSL rise, compared to 39.6% under RSL fall—a difference of 20 percentage points (Fig. 1e). A relationship of similar magnitude is observed for individual wetland types. For salt marshes, the proportion of net loss increases from 27.5% under RSL fall to 35.7% under RSL rise (Fig. 1f), whereas for mangroves it rises only slightly, from 67.1 to 69.3% (Fig. 1g). In contrast, the stable fraction (defined as |RRAC|<0.01% yr^{-1}) is smaller under RSL rise (14.8%) than under fall (37.5%), while the proportions of net gain differ by less than 3% (Fig. 1e). This pattern suggests a potential shift from stable to loss states when RSL transitions from falling to rising. In other words, although multiple factors contribute to tidal wetland loss[2,38–41], the shift from negative to positive RSL change increases the likelihood of net wetland loss. Based on this rough estimate, and considering that over 90% of global wetland extent currently lies in regions with rising RSL at a median rate of ~4 mm yr^{-1} (Fig. 1a–d), tidal wetlands have faced elevated loss risk over the past two decades.

Relative sea-level change rate threshold for abrupt wetland loss

We find a clear nonlinear declining trend and threshold behavior in tidal wetland area change for increasing RSL rise (Fig. 2a, d). These patterns are supported by two complementary statistical representations across the RSL change gradient: (1) binned fractions by change sign and (2) binned means and medians of area change magnitudes. The overall decline is reflected by an increasing proportion of loss, rising from 41% (21–61%, 66% uncertainty range, i.e., IPCC *likely range*[42]) at the bin of −14 to −13 mm yr^{-1} to 82% (57–100%, *likely range*) at 13–14 mm yr^{-1} (Fig. 2a). In contrast, the stable fraction holds a higher proportion under RSL fall than under RSL rise, peaking at 60% (53–67%, *likely range*) at bin of −9 to −8 mm yr^{-1}, then dropping to 17% (14%–19%, *likely range*) at 0–1 mm yr^{-1} and falling to zero at 12–13 mm yr^{-1} (Fig. 2a). This indicates that the probability of maintaining stability decreases with increasing RSL rise. Moreover, linear trends fitted to both binned medians and binned means show a >95% probability of being negative (Fig. 2d and Table 2), further corroborating the overall decline. The nonlinear trend is well captured by a cubic regression ($R^2 = 0.81$ for a representative fit to the ensemble-median binned RRAC values) for all tidal wetlands larger than 1 km^2 (Fig. 2d). Accounting the uncertainty, the fitted cubic curve shows an 88% probability of a declining trend in its tail (Fig. 2d and Table 2), indicating the likely existence of a high RSL rise rate threshold beyond which loss rate accelerates.

We define the threshold θ as the RSL rise rate at which wetland loss abruptly accelerates. To identify θ, we examine the bin-wise first-order differences of ensemble medians for loss fraction, mean RRAC, and median RRAC. The threshold is marked by the first bin where these differences break from zero-centered oscillations to exceed all preceding magnitudes (Supplementary Fig. 1). We adopt the maximum θ across the three indicators, which represents the latest plausible onset of accelerated loss, and yields 9 mm yr^{-1} for tidal wetlands (Fig. 2d and Supplementary Fig. 1). Beyond 9 mm yr^{-1}, loss fraction differences remain positive while RRAC differences plunge negative; below it, all differences fluctuate around zero (Supplementary Fig. 1a–c). These contrasting patterns indicate that tidal wetlands can self-adjust laterally under moderate RSL rise rates but collapse once the threshold is exceeded. This behavior is consistent with the one-dimensional numerical model of ref. 27, which shows an abrupt decline in marsh width change rate around 8–9 mm yr^{-1}. In that model, physiological mortality overwhelms compensatory landward expansion, inducing an inundation regime that becomes independent of local topography.

Segmented robust linear regression further verifies the trends identified above. Across all wetlands and RSL change rates, we find an average area loss slope of −0.0037% mm^{-1} (−0.0041 to −0.0033, 90% uncertainty range, i.e., IPCC *very likely range*[42]) (Fig. 3a and Table 3). This means a net loss of approximately 4% of global tidal wetland area per meter of RSL rise. However, the rate ranges matter as well, as slopes estimated for separate RSL change rate intervals show marked differences. Within the <0 and 0–θ (0–9 mm yr^{-1}) intervals, the slopes are weakly negative, with values of −0.0020% mm^{-1} (−0.0030 to −0.0011, *very likely range*) and −0.0027% mm^{-1} (−0.0041 to −0.0013, *very likely range*), respectively (Fig. 3a). Beyond the threshold, however, the slope steepens to −0.0213% mm^{-1} (−0.0535 to −0.0002, *very likely range*), which is eight times larger in magnitude than that in the 0–θ interval and six times larger than the full range (Fig. 3a). In addition, Monte Carlo-based comparisons indicate probabilities exceeding 90% that the >θ slope is steeper than those in the full-range, <0, and 0–θ intervals (Table 3). Using the >θ slope estimate, an intact tidal wetland would lose ~90% of its area with 4200 mm of RSL rise, which could occur within 470 years under a constant RSL rise rate of 9 mm yr^{-1}, noting that this presents a rough estimate.

We also find global loss of tidal wetlands outside the effects of RSL rise. The loss fractions across all valid RSL rise rate bins exceed 50% (Fig. 2a), and the value of the fitted curve at zero rate of RSL change indicates a net loss rate of −0.007% yr^{-1} (−0.017 to 0.003, *likely range*) (Fig. 2d). In addition, the intercept of the linear regression across the full RSL change range is −0.040% yr^{-1} (−0.042 to −0.039, *very likely range*) (Table 3). This likely reflects the influence of non-RSL drivers, such as human activities[2,38,41] and climatic disturbances[39,40,43].

https://doi.org/10.1038/s41467-026-76031-3

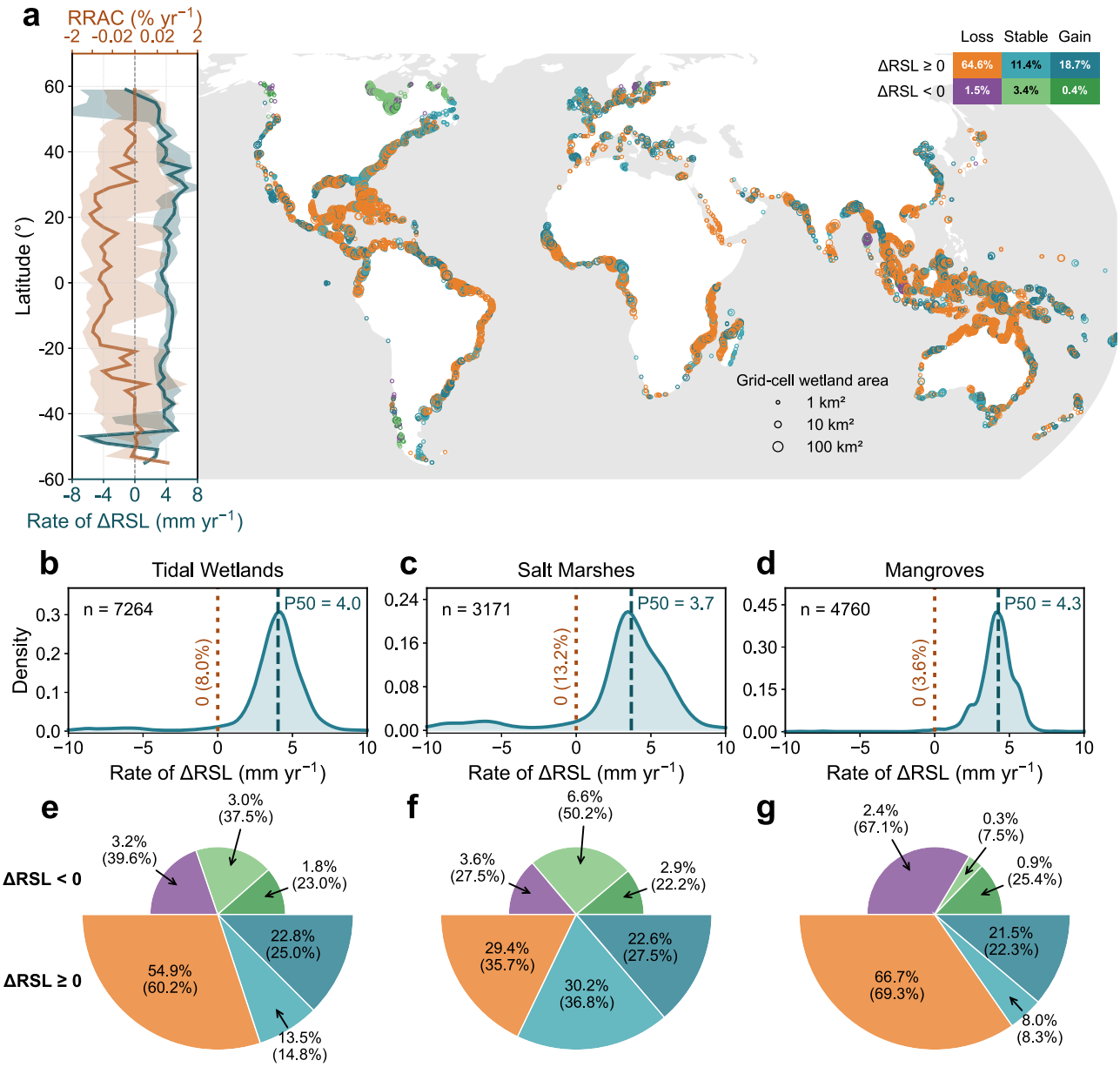

Fig. 1 | Global distribution of tidal wetland change and relative sea-level change over the past two decades. a Spatial distribution of the relative rate of net area change and relative sea-level change at 0.25° resolution. Circle size indicates total tidal wetland area per grid cell, and color denotes the bivariate classification of wetland change (loss, stable, and gain) and relative sea-level change direction (rise or fall). The left panel shows medians (solid lines) and 66% uncertainty ranges (shaded) binned by 2° latitude. Percentages in the bivariate legend (upper right) report area-weighted proportions of the six change categories. Base map data are from Natural Earth in the public domain. Probability density function of relative sea-level change for **b** all tidal wetlands, **c** salt marshes, and **d** mangroves. Orange and blue dashed lines indicate the proportion of grid cells with negative rate and the median change rate, respectively. Semi-circular pie charts (**e**–**g**) show the proportion of grid cells across the six categories for tidal wetlands **e**, salt marshes **f** and mangroves **g**, accounting for unequal areas under relative sea-level fall versus rise. Upper values indicate percentages across all six categories (summing to 100%); values in parentheses show proportions within each RSL condition (fall or rise), with each side summing to 100%. Only grid cells with >1 km² of tidal wetland in both the initial and final years are included.

Despite the influence of non-RSL drivers, RSL rise remains a discernible driver of tidal wetland area loss via direct inundation. In contrast to RRAC, which reflects net area change, RROW isolates inundation-related loss and displays a greater propensity for both an overall declining trend and nonlinear behavior, with probabilities for both two trends approaching 100% (Table 2 and Supplementary Fig. 2). Applying the same threshold detection method, we identify a global threshold of -8 mm yr^{-1} for RROW (Supplementary Fig. 2). Beyond this point, the slope of RROW relative to RSL rise rate steepens with 100% probability compared to preceding intervals (Supplementary Table 2), increasing from 0.0006% mm^{-1} (0.0003 to 0.0008, *very likely range*) to 0.0105% mm^{-1} (0.0048 to 0.0185, *very likely range*)—an approximately 18-fold intensification (Supplementary Fig. 3). These high probabilities indicate that as RSL rise rates exceed a critical threshold, the risk of wetland loss driven directly by RSL inundation inevitably escalates.

Salt marshes versus mangroves

Comparing salt marshes and mangroves, we find comparable thresholds in RSL rise rate for net area change in both ecosystems, at approximately 9 mm yr^{-1} (Fig. 2e, f). The probabilities of a steepening slope when shifting from the 0–9 mm yr^{-1} interval to rates >9 mm yr^{-1} is

https://doi.org/10.1038/s41467-026-76031-3

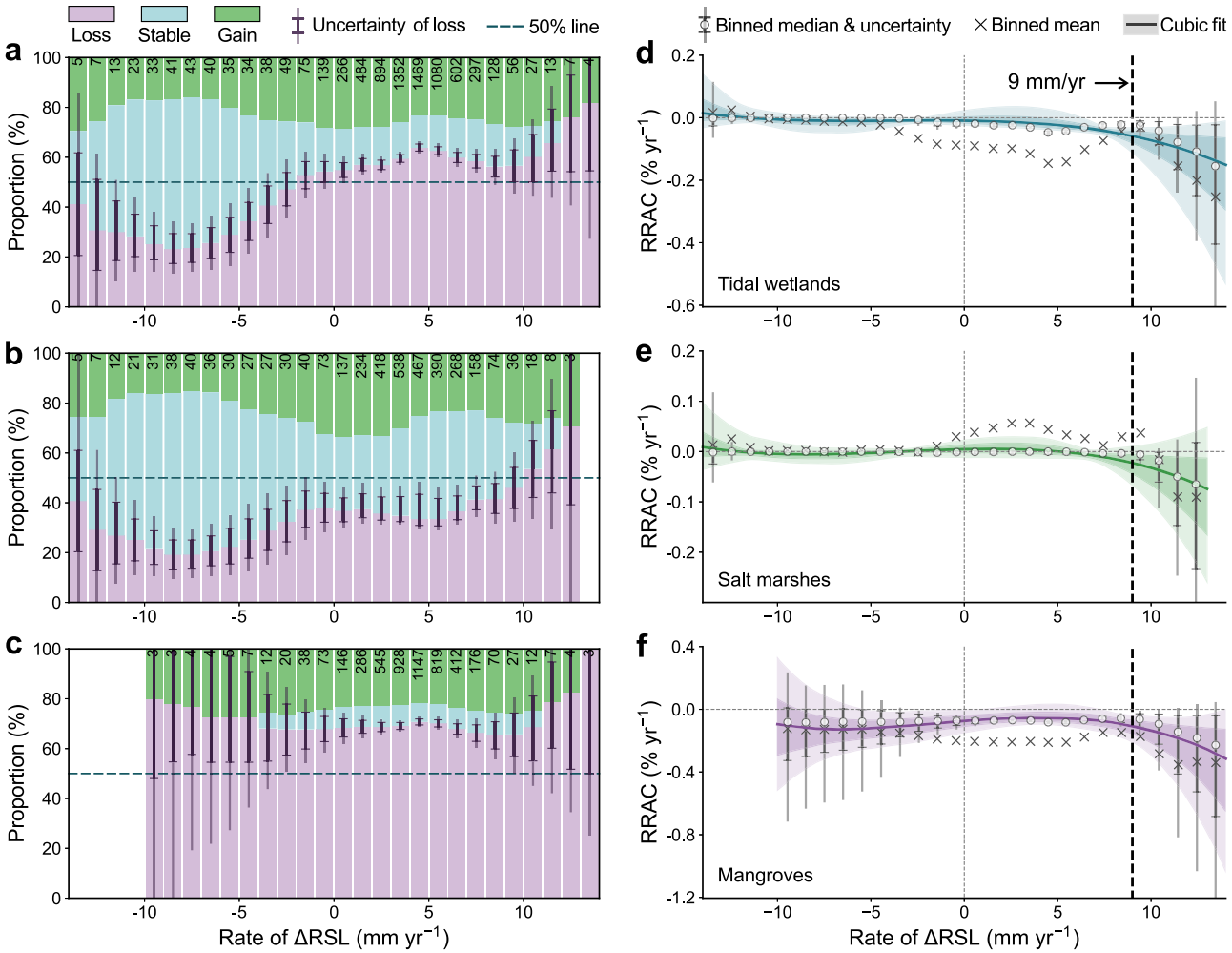

Fig. 2 | Effect of relative sea-level change on wetland surface area change. Proportions of area change classified as loss, stable or gain per millimeter of relative sea-level change are shown for **a** all tidal wetlands, **b** salt marshes, and **c** mangroves. Numbers above bars indicate cell counts in each bin. The horizontal blue dashed line marks the 50% level. Darker and lighter error bars denote the uncertainty range of 66% (*likely range*) and 90% (*very likely range*), respectively. Relative rate of net area change as a function of relative sea-level change rate are shown for **d** all tidal wetlands, **e** salt marshes and **f** mangroves. Circles and crosses denote the medians of binned medians and binned means, respectively. The grey error bars represent the 66 and 90% uncertainty ranges of binned medians. The black vertical dashed line marks the threshold position (see Supplementary Fig. 1 for detailed identification). The colored curves show cubic fits to the binned medians, with darker and lighter shaded envelopes indicating the 66 and 90% uncertainty ranges. Calculations are based on 0.25° grid cells, including only cells with total wetland area > 1 km^2 and bins containing more than three grid cells.

Table 2 | Probability of loss intensification in binned medians and means of RRAC and RROW across RSL change rate bins using different fitting methods (for grid cells with total wetland area >1 km²)

Type	RRAC (net change)		RROW (loss to open water)	
	Probability of a declining linear trend	Probability of tail decay in cubic fits	Probability of a rising linear trend	Probability of tail rise in cubic fits
Tidal wetlands	98.4%	87.6%	100.0%	99.5%
	95.7%	74.7%	100.0%	95.3%
Salt marshes	89.4%	85.2%	100.0%	100.0%
	69.7%	86.7%	100.0%	99.6%
Mangroves	67.5%	85.8%	80.0%	95.9%
	79.9%	71.7%	97.9%	88.6%

For each wetland type, the upper and lower rows correspond to fits using binned medians and binned means, respectively. Declining RRAC and rising RROW linear trends indicate overall intensifying loss with increasing RSL change rate; cubic fits show RRAC tail decay and RROW tail rise, suggesting nonlinear intensification and potential threshold effects.

76% for salt marshes and 86% for mangroves (Fig. 3b, c, and Table 3). When considering inundation-related loss alone, abrupt acceleration in loss rate is more likely to occur at ~8 mm yr^{-1} (Supplementary Fig. 3d–i), with the probability of slope increase from the 0–8 to the >8 mm yr^{-1} interval approaching 100% for both ecosystems (Supplementary Table 2). Threshold behavior is further supported by cubic fits: RRAC shows >85% probability of tail decay (i.e., accelerated net area loss) in both wetland types, and RROW indicates 100% probability of tail rise (i.e., accelerated conversion to open water) in salt marshes and 96% in mangroves (Table 2). These consistent threshold behaviors point to a close functional similarity between salt marshes and mangroves under high RSL rise.

Salt marshes and mangroves differ in their pre-threshold loss dynamics. Within the RSL rise rate interval (0–θ), regression slopes for salt marshes exhibit a negative 90% uncertainty range (−0.0015 to −0.0005% mm^{-1}), while mangroves show a broader 90% uncertainty range spanning zero (−0.0017 to 0.0017% mm^{-1}) (Fig. 3b, c, and Table 3). Moreover, salt marsh loss proportion increases by 5 percentage points (from 37% to 42%) from the 0–1 to the 8–9 mm yr^{-1} bin, whereas mangrove loss proportion decreases by 3 percentage points

https://doi.org/10.1038/s41467-026-76031-3

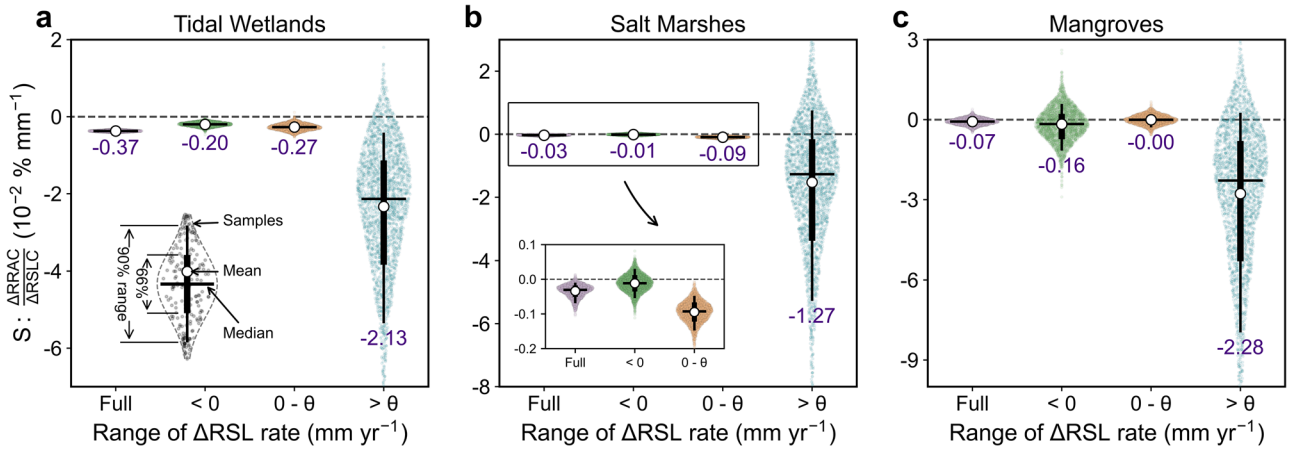

Fig. 3 | Robust regression slopes of the relative rate of wetland area change versus the relative sea-level change rate across different rate intervals. Results are shown for four relative sea-level change rate intervals: full range, <0, 0–θ, and >θ: **a** all tidal wetlands, **b** salt marshes, and **c** mangroves. θ denotes the rate threshold, identified as 9 mm yr^{-1} here. The slope quantifies the percentage change in wetland area (% yr^{-1}) and per millimeter of relative sea-level rise (mm yr^{-1}), following cancellation of the common time unit. In each violin body, the thick and thin vertical black lines represent the 66% and 90% uncertainty ranges, respectively; the white dot represents the mean, and the black horizontal line represents the median. Each colored scatter point represents the result of a single Monte Carlo simulation. The inset provides an enlarged view of the Full-range, <0 and 0–θ intervals. Purple values indicate the median slope value of each group. Grid cell counts and pairwise comparison probabilities for each interval are reported in Table 3.

Table 3 | Slopes, intercepts, and slope comparison probabilities from robust linear regressions (for the relative rate of area change against the relative sea-level change rate)

(θ = 9)	ΔRSL interval (mm/yr)	Number of cells and proportion	Area proportion	Slope (×10^{-2} %/mm)	Intercept (×10^{-2} %/yr)	Probability of slopes comparison	
Tidal wetlands	Full	7264	—	−0.37 (−0.39, −0.35) [−0.41, −0.33]	−4.03 (−4.14, −3.92) [−4.22, −3.85]	(Full) > (>θ)	90.6%
						(<0) > (>θ)	92.9%
						(0–θ) > (>θ)	92.0%
	<0	580 (8.0%)	7.2%	−0.20 (−0.25, −0.15) [−0.30, −0.11]	−1.96 (−2.44, −1.54) [−2.79, −1.26]	(Full) > (0–θ)	7.3%
						(<0) > (0–θ)	75.9%
						(Full) > (<0)	0.9%
	0–θ	6572 (90.5%)	89.7%	−0.27 (−0.35, −0.19) [−0.41, −0.13]	−4.68 (−5.04, −4.32) [−5.29, −4.08]		
	>θ	112 (1.5%)	3.1%	−2.13 (−3.84, −0.78) [−5.35, −0.02]	14.71 (0.52, 32.35) [−7.72, 46.95]		
Salt marshes	Full	3171	—	−0.03 (−0.05, −0.02) [−0.07, −0.01]	−0.21 (−0.48, 0.01) [−0.65, 0.13]	(Full) > (>θ)	77.6%
						(<0) > (>θ)	78.1%
						(0–θ) > (>θ)	76.3%
	<0	420 (13.2%)	18.5%	−0.01 (−0.04, 0.01) [−0.05, 0.03]	−0.20 (−0.42, 0.01) [−0.59, 0.16]	(Full) > (0–θ)	96.8%
						(<0) > (0–θ)	98.7%
						(Full) > (<0)	17.8%
	0–θ	2684 (84.6%)	70.6%	−0.09 (−0.12, −0.07) [−0.15, −0.05]	0.05 (−0.30, 0.42) [−0.54, 0.67]		
	>θ	67 (2.1%)	10.9%	−1.27 (−3.37, 0.25) [−5.28, 1.40]	9.53 (−5.79, 30.15) [−17.55, 48.79]		
Mangroves	Full	4760	—	−0.07 (−0.19, 0.05) [−0.28, 0.13]	−10.46 (−10.95, −9.96) [−11.33, −9.58]	(Full) > (>θ)	86.0%
						(<0) > (>θ)	83.8%
						(0–θ) > (>θ)	86.3%
	<0	173 (3.6%)	4.0%	−0.16 (−0.73, 0.39) [−1.16, 0.82]	−11.23 (−14.04, −8.73) [−16.33, −7.10]	(Full) > (0–θ)	28.5%
						(<0) > (0–θ)	39.1%
						(Full) > (<0)	56.3%
	0–θ	4530 (95.2%)	95.2%	−0.00 (−0.17, 0.17) [−0.29, 0.28]	−10.69 (−11.43, −9.96) [−11.95, −9.44]		
	>θ	57 (1.2%)	0.7%	−2.28 (−5.30, −0.27) [−7.97, 0.87]	10.11 (−12.55, 41.07) [−26.98, 67.36]		

Values in parentheses indicate the *likely range*; values in square brackets indicate the *very likely range*.

https://doi.org/10.1038/s41467-026-76031-3

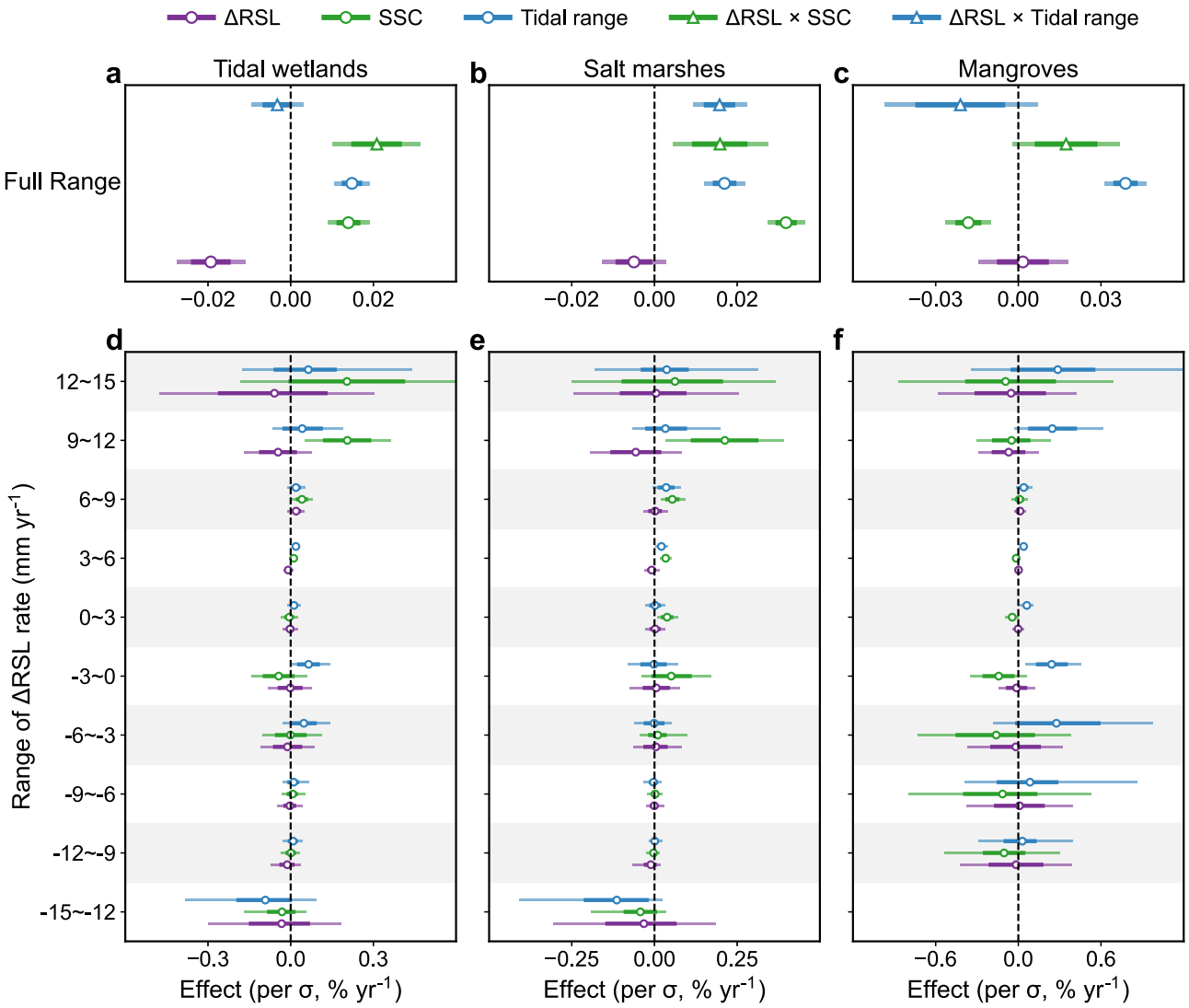

Fig. 4 | Effects of tidal range and sediment availability on wetland area change under relative sea-level change. Global multiple linear regressions incorporating interaction terms between relative sea-level change rate and each of tidal range and suspended sediment concentration, for **a** all tidal wetlands, **b** salt marshes, and **c** mangroves. Stratified multiple linear regressions excluding interaction terms, with effects estimated within 3 mm yr^{-1} intervals of relative sea-level rate for **d** all tidal wetlands, **e** salt marshes, and **f** mangroves. Circles denote mean coefficients of independent terms; triangles denote mean coefficients of interaction terms. Horizontal thick dark lines represent the 66% uncertainty range (aligned with the IPCC *likely range*), while thin, light lines represent the 90% uncertainty range (IPCC *very likely range*). The corresponding standard errors (σ) values are provided in Supplementary Table 3.

(from 68 to 65%) over the same interval (Fig. 2b, c). Further evidence of loss acceleration in salt marshes is provided by the probability of a rising linear trend in binned median RROW: 100% versus 80% in mangroves (Table 2). These results suggest that, before reaching the threshold collapse of abrupt loss, salt marshes experience a low but persistent rate of area loss under RSL rise, whereas mangroves exhibit greater oscillatory behavior.

Another notable difference is the observed loss in the absence of RSL change. Mangroves have experienced loss independent of RSL change: the constant term of the cubic fit is −0.075% yr^{-1} (−0.150 to −0.005, *very likely range*) (Fig. 2f). This pattern is consistent with previous studies attributing substantial mangrove decline to socio-economic drivers[38,41] and extreme storm events[40,43]. In contrast, the constant term for salt marshes is slightly positive, 0.004% yr^{-1} (−0.012 to 0.023, *very likely range*) (Fig. 2e), suggesting minor gains in the absence of RSL rise. Under increasing RSL change rates, however, this slight gain quickly reverses into a net loss (Fig. 2b). Hence, mangroves are more strongly affected by non-RSL factors than salt marshes in terms of loss risk.

Roles of tidal range and sediment availability

Tidal range exhibits a positive association with RRAC across tidal wetlands (Fig. 4a). A one-standard-deviation increase in tidal range (σ = 1.88 m, Supplementary Table 3) corresponds to an increase in RRAC of 0.015% yr^{-1} (*very likely range*: 0.011–0.019), equivalent to 0.008% yr^{-1} (0.006–0.011) per meter. This relationship persists when salt marshes and mangroves are analyzed separately (Fig. 4b, c). However, the interaction between tidal range and RSL change rate differs between the two ecosystems (Fig. 4a–c). In salt marshes, a larger tidal range buffers RSL-driven area loss (coefficient: 0.009–0.022, *very likely range*), whereas in mangroves it weakens this buffering effect (coefficient: −0.037 to −0.005, *likely range*). Multiple linear regressions, stratified by 3 mm yr^{-1} intervals of RSL change rate, clarify this divergence. For salt marshes, the effect of tidal range is negative where RSL change rate <0, becomes positive in the 3–6 mm yr^{-1} interval, and remains positive at higher RSL change rates (Fig. 4e). In contrast, mangroves show a diminished positive effect across 0–9 mm yr^{-1}, which strengthens beyond the ~9 mm yr^{-1} threshold (Fig. 4f).

Sediment availability, represented by SSC, also shows a positive association with tidal wetland area change at the aggregated level, with a standardized coefficient increase of 0.014 (0.009–0.019, *very likely range*), equivalent to 0.0013% yr^{-1} per g m^{-3} increase in SSC (Fig. 4a). However, this effect differs markedly between wetland types. In salt marshes, SSC exhibits a consistently positive effect (0.027–0.036, *very likely range*; Fig. 4b), but negative in mangroves (−0.026 to −0.010, *very likely range*; Fig. 4c). Notably, the SSC-RSL change rate interaction term is likely positive in both wetland types (salt marshes: 0.009–0.022; mangroves: 0.006–0.029; *likely range*; Fig. 4b, c), indicating that higher SSC generally mitigates RSL-driven area loss despite the contrasting standalone effects of SSC. This pattern is further supported by stratified regressions that exclude the interaction term, in which the effect of SSC shifts from negative or near-neutral when RSL change rate <0 to positive when RSL change rate >0 (Fig. 4d–f).

Overall, these results suggest that tidal range generally exerts a positive effect on tidal wetland area change, while SSC shows divergent standalone effects: a positive effect in salt marshes but a negative in mangroves. Moreover, both influences become more pronounced in resisting RSL-driven loss under higher RSL change rates, acting as compensatory mechanisms under accelerating RSL rise.

Discussion

Our observations confirm that lateral adjustment can partially mitigate tidal wetland area loss induced by relative sea-level rise. Of the two area-change metrics we quantified, conversion to open water represents the lateral cumulative effects of inundation processes, whereas net area change integrates overall lateral processes. Under low-to-moderate RSL rise rates, both metrics show resilience, primarily attributable to maintenance or increase of elevation capital[44,45]: organic and mineral accumulations raise surface elevation, thereby offsetting RSL rise and reduce submergence risk[5,13,27,46]. Where external sediment supply is sufficient, seaward progradation is also enabled, particularly in deltaic settings[47–49], such as the eastern section of the Ganges-Brahmaputra-Meghna Delta[50] and the Changjiang Delta[51].

An additional buffering mechanism operates under high RSL rise rates through integrative lateral reorganization. Although both metrics exhibit nonlinear responses, RRAC shows a higher area-based threshold (~9 mm yr^{-1} versus ~8 mm yr^{-1}) and a lower probability of decline (>66%, *likely*) under accelerating RSL rise compared to RROW (>95%, *extremely likely*) (Tables 2, 3, and Supplementary Table 2). This indicates that lateral reorganization, despite encompassing non-RSL-driven losses, has provided a quantifiable buffer against tidal wetland degradation over the past two decades. To further elucidate this buffering capacity, we introduce a refined area-change metric, RRAC′, defined as the relative rate of gross wetland gain minus loss to open water. RRAC′ directly quantifies the extent to which wetland gain offsets inundation-related loss. The relationship between RRAC′ and RSL change rate reveals a relatively inconspicuous threshold effect at high RSL rise rates (Supplementary Fig. 4d–f), with probability assessments differing between linear and nonlinear loss trajectories (Supplementary Table 4). This suggests that the RSL rise rate threshold for accelerated wetland loss may become obscured or shift to higher values if non-RSL-driven losses are effectively constrained. A key buffering behavior occurs when RSL rise outpaces surface elevation gain and depletes elevation capital, yet wetland area may not immediately decline if landward migration is possible (refs. 4,52–54; Supplementary Figs. 5c and 6b), and area gains can occasionally exceed losses[18]. Lateral erosion can also reallocate sediment to vertical accretion, potentially allowing wetlands to adapt to rising sea levels[45,55,56]. Additionally, wetland restoration efforts have contributed to decelerating area decline[3,57]. Collectively, global tidal wetlands may demonstrate moderate lateral resilience to accelerating RSL rise under the combined natural and anthropogenic forcing.

The loss of global tidal wetlands likely emerges as a chronic, progressive process under high rates of RSL rise. In a parallel analysis using area changes computed over successive 3-year intervals, we still detect nonlinear threshold responses in both RRAC and RROW, similar to those obtained from the two-decade analysis (Supplementary Figs. 7 and 8). This suggests that, at the global scale, degradation processes exceeding the RSL threshold emerge even at shorter timescales, rather than requiring multi-decadal observation windows to manifest. In view of the very likely existence of a secular, centennial-scale global mean sea-level rise prior to the satellite altimetry era[58,59], the detection of such phenomena over shorter periods is to be expected, even given potential time-lagged responses[6,56,60].

Wetland loss is likely to intensify further as RSL rise rates increase[61]. In recent decades, only ~3% of global wetland extent has experienced RSL rise rates exceeding the critical thresholds identified here, though these threshold estimates remain subject to considerable uncertainty (Figs. 2, 3, and Table 3). Loss proportions increase under both the RRAC and RRAC′ metrics as RSL rise rates accelerate, indicating escalating submergence risk despite their lateral buffering capacities (Fig. 2a–c and Supplementary Fig. 4a–c). In a supplementary analysis, we find that tidal wetlands experiencing both RSL rise and acceleration show higher loss proportions than those with RSL rise but deceleration (salt marshes: 41.9% vs. 29.2%; mangroves: 83.2% vs. 65.3%; Supplementary Fig. 9), underscoring heightened risk for wetlands under accelerating RSL rise over the past two decades. Under SSP3-7.0, globally averaged geocentric rates of 8 mm yr^{-1} are expected as early as 2060 (ref. 62), implying that an increasing fraction of tidal wetlands may face nonlinear abrupt collapse. Yet this projection likely represents a lower bound for deltaic regions, where anthropogenic subsidence increasingly dominates relative sea-level rise and amplifies compound coastal flooding[63].

Except for the analogous threshold response, we find relatively higher resilience of mangroves compared with salt marshes under low-to-moderate RSL rise conditions based on the loss fraction trends (Fig. 2b, c, and Supplementary Fig. 10) and uncertainty ranges (Fig. 3b, c, and Table 3). This may result from their greater capacity to build or maintain elevation through high root biomass production[23]. Another contributing factor is that mangroves typically develop less extensive channel networks[64], making them comparatively less susceptible to seawater intrusion. Given this higher resilience, the poleward expansion of mangroves into salt marshes under global warming[65,66] could act as a natural adaptation mechanism for tidal wetlands to cope with increasing RSL rise. Nevertheless, despite their advantages, mangroves still experience larger overall losses than salt marshes (Figs. 1f, g, 2b, c, and Supplementary Fig. 6c, d) and are exposed to higher RSL rise rates (Fig. 1c, d), indicating the need for targeted management to mitigate additional damages[38,41,67].

Natural factors, such as tidal range and SSC, can partially mitigate the threat posed by accelerating RSL rise. For RRAC, our observed positive effect of tidal range is consistent with previous findings (Fig. 4; refs. 17,68–70). A larger tidal range prolongs inundation duration and increases water depth, thereby facilitating vertical sediment deposition in low-lying zones[71] and promoting the maintenance of elevation capital[44]. It also provides broader accommodation space for sediment accumulation and vegetation establishment[4,13]. In salt marshes, SSC exerts a similarly positive influence, enhancing vertical accretion and lateral expansion[9,68,72].

By contrast, the negative RRAC–SSC association observed in mangroves is counterintuitive. To isolate this effect from confounding lateral processes, we conduct an analogous multiple linear regression on RROW. Notably, both wetland types exhibit a positive RROW–SSC relationship (Supplementary Fig. 11b, c), indicating that inundation-related loss actually accelerates under high-SSC settings. This apparent paradox may arise from several mechanisms. First, in highly turbid estuaries, coastal vegetation has been actively removed to maintain

navigable channels or open tidal flats (e.g., mangroves in New Zealand[73]), or to eradicate fast-growing invasive species for ecological safety (e.g., *Spartina alterniflora* in Changjiang estuary[74]). Second, excessive sediment deposition under high SSC can suppress plant growth or even induce mortality through hypoxic stress[75–77]. Alternatively, if viewed from a sedimentary perspective, the positive RROW–SSC relationship could reflect sedimentary signatures of retreating wetland margins: extensive inundation-related wetland loss elevates local turbidity via resuspension from exposed substrates[78], and landward reallocation of this sediment promotes elevation gain[45]—which would explain why RRAC in salt marshes remains positively correlated with SSC. For mangroves, however, anthropogenic disturbance likely remains the dominant driver of loss[41], thereby masking this compensatory signal. Collectively, the current dataset cannot fully discriminate natural drowning from anthropogenic disturbances, and regression analysis alone cannot establish causality. Despite this limitation, our findings provide strong correlational evidence that the buffering capacity of lateral reorganization is mediated by both physical setting (tidal range, SSC) and local human activities, underscoring the need for site-specific risk assessments.

Our results further suggest the importance of vegetation itself in conferring resistance to sea-level forcing in tidal wetlands. Across most ranges of RSL rise rates (from the −12 to −9 to the 3–6 mm yr^{-1} intervals), both types of tidal wetlands exhibit a general neutral response (Fig. 4d–f), likely reflecting the intrinsic adaptive capacity of vegetation[23,27]. Once this quasi-steady state is exceeded, external factors, tidal range and SSC, become increasingly important in buffering the erosive threats associated with accelerating RSL rise[32]. This shift suggests a potential transition in wetland adjustment mechanisms from an "internal" (vegetation-dominated) mode to an "external" (environmentally mediated) response, until these compensatory processes can no longer keep pace[68]. Such a transition may explain the enhancement of the positive effects of tidal range and/or SSC observed under the highest RSL rise rate intervals in Fig. 4d. Given that tidal range cannot be actively modified, safeguarding existing vegetation remains critical for coastal protection, while managing anthropogenic sediment supply offers an additional actionable strategy where feasible.

Our interpretation of wetland vulnerability based on these results may be conservative. First, defining thresholds as the maximum across multiple metrics could overestimate the critical rates (Supplementary Fig. 1). Abrupt loss acceleration may exist at a preceding point, for example, mangrove binned mean RROW increases dramatically at ~7 mm yr^{-1} (Supplementary Fig. 2h). Moreover, a slight net loss trend is already evident below the threshold (manifested as a decline in Fig. 3 and a rise in Supplementary Fig. 3), implying that acceleration effects cannot be disregarded even at low-to-moderate RSL rise rates[60]. Second, the thresholds observed here exceed most reported vertical thresholds from SET-MH sites (Table 1). Although vertical accretion and lateral area change show a modest correlation (Pearson's $r = 0.20$, $p = 0.014$; Supplementary Fig. 12), our reliance on 30-m wetland change data may obscure fine-scale variations and inflate threshold estimates. Furthermore, area change is an inherently lagged indicator relative to vertical processes: even after vertical accretion falls behind RSL rise, high-elevation wetlands require time to become inundated before elevation capital is exhausted[6,60,79]. Discrepancies in the RSL data benchmarks between this study and prior observations may also introduce additional bias[80]. Third, the relatively short observation period (~20 years) and the use of linear trend estimation may mask ongoing accelerated losses that are not yet apparent[60], especially given that the global sea-level rise rate has doubled over the past three decades[81]. Fourth, local resilience may be overestimated because regional variability is smoothed in a globally aggregated response, potentially obscuring site-specific sensitivities and adaptation limits[4,53,78].

We acknowledge that threshold estimates are definition-dependent. Our approach identifies abrupt loss acceleration positions, whereas previous vertical studies used submergence proportion to detect thresholds aligned with IPCC *likely ranges*[14,20,82] (Table 1). Applying the latter method to the loss fractions in Fig. 2b, c yields substantially higher thresholds: 12 mm yr^{-1} (66% for salt marshes) and 13 mm yr^{-1} (90% for mangroves). These values appear overly optimistic, underscoring the urgent need to establish which definition best captures threshold behavior (see Supplementary Discussion for details).

Several methodological uncertainties warrant consideration. Although our grid-cell RSL change rates correlate strongly with tide-gauge trends (Pearson's $r = 0.88$, $p < 0.001$, slope ≈ 1; Supplementary Fig. 13a), inherent limitations persist. Vertical land motion (VLM) estimates are constrained by sparse and uneven GNSS and tide-gauge coverage, short and noisy InSAR time series, and methodological inconsistencies[37]. Shallow subsidence above GNSS foundation depths can bias VLM rates negatively[83], potentially leading to underestimated RSL change rates and loss thresholds. Additional uncertainty arises from gaps in the VLM data, mostly in regions, such as northwestern North America, northern and northeastern Eurasia, and the Philippine Archipelago, where GNSS stations and tide-gauge records are unavailable (Supplementary Fig. 14 and Supplementary Table 1). There are also limitations in delineating marsh extent at high latitudes (Supplementary Fig. 15c, d). Episodic tectonic events and strong local-to-regional heterogeneity can introduce additional variability of several millimeters per year[37]. Notably, a recent study synthesized multi-source data to close spatial gaps[84]; future work with this new VLM map may advance our understanding of wetland responses to RSL rise. Finally, although our convolution-based interpolation performs high accuracy at the kernel centers (Supplementary Fig. 14b, c), uncertainty in VLM and geocentric sea-level rise in surrounding wetland grid cells may still be underestimated.

Uncertainties also persist in RRAC (relative rate of area change) estimation. Although our uncertainty-bound resampling method recovers the original range of area change with >92% fidelity (Supplementary Fig. 16), unknown error distributions and the limited spatial explicitness of uncertainty estimates may leave residual biases. Global-scale datasets may inaccurately resolve coastal wetlands regionally. For example, Campbell et al.[34] likely underestimates historical salt marsh expansion along the U.S. mid-Atlantic and Gulf Coast of Florida, diverging from region-focused studies[85,86]. Incorporating no-change areas introduces noise from cross-source delineation discrepancies, and incomplete temporal overlap further compounds rate estimation uncertainty. Additionally, the choice of grid-cell wetland extent cutoff and analysis resolution introduces uncertainty. To evaluate these effects, several parallel analyses were performed. Binary gain-loss analysis on individual datasets (ignoring wetland extent cutoff to exclude biases from total-extent datasets) reproduces the increasing loss proportions under RSL rise rates shown in Fig. 2b, c (Supplementary Fig. 10). Repeating the Fig. 2e, f analyses across individual datasets further validates the nonlinear RRAC threshold trends (Supplementary Fig. 17). Moreover, the key findings in Fig. 2 remain consistent when shifting the grid-cell wetland extent cutoff from 1 to 0.1 km^2 (Supplementary Fig. 18) and the analysis resolution from 0.25° to 0.125° (Supplementary Fig. 19). These analyses support the robustness of our main conclusions despite multi-source uncertainties.

In conclusion, we reveal a global nonlinear response in tidal wetland area change with increasing relative sea-level rise, with thresholds of apparent loss acceleration of ~9 mm yr^{-1} for overall lateral dynamics and ~8 mm yr^{-1} for inundation-related loss. Across all tidal wetlands, we find a loss rate of approximately −0.0037% per mm of RSL rise. However, this loss rate depends strongly on the RSL rise rate and increases sharply beyond the threshold. Mangroves appear more resilient than

salt marshes under moderate rates of RSL rise, which may arise from their biomass productivity. Our findings provide important insights into tidal wetland vulnerability under accelerating relative sea-level rise. Looking forward, future studies should explicitly integrate lateral processes, species-specific interactions, longer-term response monitoring and heterogeneous coastal boundary conditions to enable more robust and site-specific projections.

Methods

Overview

To investigate the global relationship between tidal wetland area change and RSL change, we compiled multiple up-to-date global datasets covering the first two decades of the 21st century. Our analysis consisted of two main components (Supplementary Fig. 20): (1) construction of global maps of RSL change and tidal wetland area change, comprising overall lateral dynamics (net change) and inundation-related loss (area directly converted to open water) and (2) assessment of the relationship between wetland dynamics and RSL change. All datasets were standardized to a common spatial resolution of 0.25°, and uncertainties from major sources and processing steps were carefully quantified. Based on these maps, the association between tidal wetland dynamics and RSL change was assessed using different quantitative approaches, including classification-based probability analyses and continuous variable assessments. Key natural drivers previously identified as regulating tidal wetland responses—tidal range and sediment availability (refs. 4,32,68)—were included to evaluate their role in modulating these responses. Analyses were conducted separately for salt marshes, mangroves, and all tidal wetlands combined. Finally, we tested the sensitivity of our main results to variations in temporal span, spatial settings, and dataset configuration.

Calculating the relative rate of area change (RRAC and RROW)

We reconstructed global tidal wetland area-change maps by integrating four high-resolution (30 m) Landsat-derived datasets: SMC (Campbell et al.[34]) and SMM (Murray et al.[3]) for salt marshes, and MGB (Bunting et al.[35]) and MGM (Murray et al.[3]) for mangroves (Supplementary Table 5), in order to maximize observed change detection and cross-validate the robustness of global patterns against localized errors. All datasets span at least two decades (1996–2019 to 2000–2019), allowing estimation of two-decade changes (Supplementary Table 5). Spatial gains and losses were originally reported over different temporal intervals: SMC was divided into four 5-year periods[34], SMM and MGM into seven 3-year periods[3], whereas MGB starts in 1996, with the next available observation in 2007 (ref. 35). To harmonize these datasets, spatial gains and losses were aggregated within each dataset over its full observation period and summarized within each 0.25° grid cell. Gridded gross gains and losses were then used to calculate annual rates of absolute net area change (RAC).

RAC estimated from different datasets in overlapping grid cells are positively correlated (salt marshes: SMM–SMC, $r = 0.52$, $p < 0.001$; mangroves: MGM–MGB, $r = 0.71$, $p < 0.001$; Supplementary Fig. 15a, b), indicating that combining the datasets is reasonable for further analyses. For integration, we retained RAC estimates from datasets with longer temporal coverage (SMM for salt marshes and MGB for mangroves) in overlapping grid cells, while non-overlapping grid cells used the available dataset. This procedure produced a global 0.25° map of grid-level tidal wetland area change (Supplementary Fig. 15d).

To obtain the grid-cell baseline area, we performed identical zonal aggregation to the most recent global extent datasets for mangroves[87] and salt marshes[88] (10–30 m spatial resolution; Supplementary Fig. 15c), both for the year 2020. We identified no-change grid cells as those with zero gain and zero loss in the baseline area datasets, and included them as valid observations. The inclusion of no-change cells is essential for assessing terrestrial ecosystem vulnerability to climate change[89] and adaptive capacity of coastal ecosystems to RSL change[20]. To ensure consistent coverage, we excluded latitudinal segments where any of the three datasets (gain, loss, and total extent) had a discontinuity exceeding 3°. The remaining overlapping continuous ranges across all three datasets were retained as the valid latitudinal extent. These procedures were applied to tidal wetlands (combined) and separately to salt marshes and mangroves. The final dataset thus comprises all grid cells exhibiting gain, loss, or no change for each wetland type.

To enable comparison among grid cells with different wetland extents, we calculated the relative rate of area change (RRAC) as follows:

$$\mathrm{RRAC}_k = \frac{\mathrm{RAC}_k}{A_{\mathrm{ref},k}} \times 100\% \tag{1}$$

where $A_{\mathrm{ref},k}$ denotes the tidal wetland area in the reference year (i.e., the initial year of each dataset) for the k-th grid cell. The reference-year area was back-calculated from the 2020 extent by subtracting the cumulative area change over the observation period. Grid-cell examples are shown in Supplementary Figs. 5 and 6.

As a counterpart to the overall lateral dynamics, we conducted a parallel analysis of direct inundation-driven wetland loss. We first obtained the 2020 global permanent surface water distribution[90]. We removed areas overlapping with the 2020 global aquaculture pond clustering[91], yielding the natural open water mask. We then intersected the loss pixels from the tidal wetland datasets with this natural open water mask to extract wetland area converted to open water. Finally, we applied the RRAC gridding procedure to calculate RROW (relative rate of conversion to open water) for each valid grid cell.

Calculating relative sea-level (RSL) change rate

RSL changes were derived by combining globally gridded vertical land motion (VLM) and geocentric (or absolute) sea-level trend (ASL) datasets. VLM trends and associated uncertainties were obtained from a recent global reconstruction capturing present-day VLM variability at 0.25° resolution for 1995–2020 (ref. 37). Geocentric sea-level trends and uncertainties were sourced from a 2° resolution dataset covering 1993–2019 (ref. 36), after filtering out individual meso-scale eddies to remove substantial variability. Together, these datasets span the full assessment period of tidal wetland area change (1996–2019), allowing wetland dynamics to be evaluated in the context of concurrent VLM and ASL trends.

To increase spatial coverage within tidal wetland regions, we implemented a convolution-based interpolation approach. The ASL dataset was first resampled from 2° to 0.25° resolution using cubic convolution. Subsequently, to fill as many missing values as possible in the tidal wetland grid cells, both VLM and resampled ASL fields were interpolated using a focal inverse-distance-weighted (IDW) scheme within a 1° moving window centered on each grid cell. To reduce spatial mismatch between RSL changes and wetland observations, grid cells without either VLM or ASL data within a 1° neighborhood were excluded. Weights were defined as:

$$w_i = \frac{d_i^{-p}}{\sum_{i=1}^{n} d_i^{-p}} \tag{2}$$

where d_i denotes the distance between the target grid cell and the i-th neighboring cell, n is the total number of cells the neighborhood, and p is the distance-decay exponent, set to 1/2 after testing $p = 2$, 1, and 1/2 and selecting the value that maximized the interpolation R^2. The central cell was assigned a weight of zero (Supplementary Fig. 14a), allowing leave-one-out cross-validation for accuracy and uncertainty assessment (see Uncertainty quantification). RSL change rates in each grid cell were then calculated as ASL change minus VLM, and

associated 1σ uncertainties were derived from the propagated uncertainty fields (Supplementary Fig. 14d, e).

We validated our grid-cell RSL change rates against tide gauge RSL trends compiled by NOAA (Supplementary Fig. 13a). For alignment, gauges with at least 20 years of valid data during the period of 1993–2020 were retained and spatially matched to the respective grid cells. To test the sensitivity of the ASL data downscaling step, another set of RSL trends was derived by using the native 0.125° Copernicus Marine Service sea surface height product while keeping the VLM component unchanged. Both RSL trend reconstructions showed similar regressions close to the 1:1 line against tide-gauge observations with relatively high correlation (Supplementary Fig. 13), indicating that downscaling from 2° negligibly affects RSL change rate reconstruction accuracy.

Uncertainty quantification

Because the datasets of tidal wetland area change, vertical land motion, and sea-level rise all carry non-negligible uncertainties, we quantified uncertainty in our results by propagating uncertainties from both data sources and processing procedures. Grid-cell uncertainty was quantified for both RRAC and RSL change by the steps below:

For the RRAC maps, grid-level uncertainty was estimated by proportionally scaling the upper and lower bounds reported in the original datasets (refs. 3,34,35; Supplementary Table 5), according to the relative magnitude of area change. Because omission and commission errors were treated differently among dataset sources, the reported uncertainty ranges of gain and loss exhibit varying degrees of asymmetry (Supplementary Table 5). As for no-change grid cells, we assigned a 1σ uncertainty of 5000 m^2, corresponding to approximately 5–6 pixels at 30-m resolution.

For the RSL change map, uncertainty was propagated across the full processing workflow using a Monte Carlo approach. Random perturbations were applied to the mean VLM and ASL trends in each grid cell according to their reported uncertainties[36,37], and the processing procedure was repeated to derive ensemble mean values and propagated uncertainty distributions. Interpolation accuracy was assessed through leave-one-out cross-validation by comparing reconstructed values with original kernel-center values. The resulting root-mean-square errors (RMSE) are 1.68 mm yr^{-1} for VLM and 0.42 mm yr^{-1} for ASL (Supplementary Fig. 14b, c). These RMSE values were treated as interpolation uncertainty and combined with the propagated uncertainty for each grid cell by summing in quadrature. Grid cells at the kernel centers retained their original values and uncertainties.

Subsequently, the resulting grid-cell-specific uncertainty estimates were further propagated into the relationship analyses. Ten thousand realizations were generated independently for each variable and grid cell based on the characteristics of their uncertainty distributions. Variables with symmetric uncertainty intervals were sampled assuming normal distributions. For area gain and loss estimates exhibiting asymmetric uncertainty ranges, gamma distributions were adopted: positively skewed intervals were sampled directly, whereas negatively skewed intervals were first reflected to a positive domain, sampled using gamma distributions, and subsequently back-transformed to the original scale (see Supplementary Method for details). The relative estimation errors of these sampling procedures are generally below 8% for reproducing the prescribed uncertainty bounds across all grid cells (Supplementary Fig. 16).

All subsequent analyses were performed iteratively across paired realizations, yielding distributions of the resulting metrics. The uncertainty of the results was assessed using empirical quantiles derived from the ensemble distributions. For characteristic metrics, the uncertainty ranges were then reported following IPCC uncertainty language conventions, with the 17th–83rd percentiles representing the *likely range* and the 5th–95th percentiles representing the *very likely range*[42].

Association analysis between RRAC and RSL changes

To retain sufficient information while minimizing errors from very small wetland patches, we applied area-based filtering prior to the association analysis. Based on data-point counts and area-fraction analyses across wetland area orders of magnitude, a minimum threshold of 1 km^2 for total wetland area per grid cell was adopted. This criterion retained 7264 valid grid cells, covering >99% of the global tidal wetland area with valid RSL change data, while excluding over 40% of all cells (Supplementary Fig. 21 and Supplementary Table 1), including 3171 salt marsh cells and 4760 mangrove cells.

Associations between RSL change and wetland area dynamics were first examined using a binned-statistics approach, considering two complementary analyses. Within each RSL change rate bin (1 mm yr^{-1}, retaining only bins with ≥3 grid cells), RRAC values were analyzed both categorically and continuously. First, for each realization, RRAC values were classified into net gain, stable, and net loss categories using a threshold of ±0.01% yr^{-1}, and the relative proportions of each category were calculated, providing a frequency-based assessment of wetland response. Second, continuous RRAC values were used to calculate mean and median per bin, and a cubic regression was fitted to the binned median values to characterize the overall response pattern. We further applied first-order differencing to the binned loss fractions and RRAC magnitudes. This quantified changes between consecutive RSL intervals and helped identify potential thresholds.

Preliminary bin analyses revealed a threshold-like response in RRAC (Fig. 2 and Supplementary Fig. 1). To further quantify this phenomenon, filtered grid-cell values were classified into RSL change rate ranges: full range, negative RSL change (<0), 0 to threshold (0–θ), and above threshold (>θ). To mitigate the influence of potentially extreme outliers arising from small reference wetland areas, Huber robust linear regression was applied to RRAC values and RSL change rates within each range[92]. The distributions of regression slopes obtained from all Monte Carlo simulations were then compared across RSL change rate ranges to quantify the confidence in the threshold behavior.

Impact analysis of tidal range and sediment availability

We explored the effects of two key factors, tidal range and sediment availability, previously identified as influencing tidal wetland responses to RSL rise[4,32,68].

Tidal range (TR) was derived from the FES2014 global tidal model (1/16° resolution), which integrates satellite altimetry, tide gauges, and hydrodynamic modeling[93]. The amplitudes of four principal tidal constituents (M2, K2, S1, and O1) were extracted, and TR was calculated as twice their sum (Supplementary Fig. 22a). For each wetland grid cell, the mean TR of the eight nearest FES2014 grid cells within 0.5° was assigned; cells lacking neighboring values were excluded from the analyses involving TR.

Sediment availability was approximated using suspended sediment concentration (SSC) from the Copernicus GlobColour Level 4 (L4) dataset[94]. This dataset provides global monthly suspended matter (SPM) estimates at 4 km resolution, derived from multi-sensor satellite observations including SeaWiFS, MODIS, MERIS, VIIRS-SNPP, and OLCI. Similar products have been widely applied in previous tidal wetland studies[4,95]. Monthly SPM data from 1999 to 2020 were averaged to obtain long-term mean values for each grid cell (Supplementary Fig. 22b). The assignment procedure was identical to that used for TR, and cells without neighboring SSC values were excluded from the SSC-based analyses.

To assess the combined effects of RSL change rate (RSLC), TR, and SSC on tidal wetland area change, we applied a multiple linear regression (MLR) approach. Independent variables were standardized using Z-scores to allow comparison of relative effects. The maximum variance inflation factor (VIF) is 2.1, less than 5, indicating acceptable multicollinearity[96]. Here, to preserve the contribution of each variable

to RRAC in the regression, we used ordinary least squares (OLS) regression. To limit the influence of a few extreme values (Supplementary Fig. 21), the absolute magnitude of change was capped at 5% yr^{-1} (values exceeding 5% yr^{-1} were set to 5% yr^{-1}). This caps the maximum growth at 100% over 20 years, affecting only 0.3% of all data points. The final model is expressed as:

$$\begin{aligned} RRAC = {} & \beta_0 + \beta_1 \widetilde{RSLC} + \beta_2 \widetilde{SSC} + \beta_3 \widetilde{TR} + \beta_4 \widetilde{RSLC} \\ & \times \widetilde{SSC} + \beta_5 \widetilde{RSLC} \times \widetilde{TR} + \varepsilon \end{aligned} \quad (3)$$

where variables with a tilde (-) denote standardized values; β_0 represents the expected RRAC when all independent variables are at their mean values; β_1 to β_3 indicate the change in RRAC (% yr^{-1}) associated with a 1σ increase in each single variable, holding others constant; β_4 to β_5 are the coefficients of the interaction terms related to RSL change rate; ε is the error term. This model was then applied to all valid data to estimate the global contributions of each variable to RRAC.

To further examine how the effects of SSC and tidal range vary across different RSL change rate ranges, we performed multiple linear regressions without interaction terms over consecutive 3 mm yr^{-1} intervals of RSL change rate. Only intervals with over 8 valid data points were retained for reliable estimation. To enable cross-interval comparison, we rescaled the coefficients by the ratio of each factor's within-interval standard deviation to the mean of its standard deviations (σ) across all intervals. This allows every coefficient to be interpreted on a common scale. By tracking changes in these effect coefficients across rate intervals, we are able to assess how the contributions of SSC and tidal range to wetland area change vary with RSL change rates.

Sensitivity analysis

To test the robustness of our main findings across selections of temporal and spatial scales and wetland datasets, we repeated the same methodological framework under alternative configurations.

Temporal coverage

To test whether our main findings depend on long-term monitoring, we applied an identical analytical framework as in Fig. 2d–f to Murray et al.'s data (ref. 3), which provides continuous 3-year change intervals (2001–2004, 2004–2007, 2007–2010, 2010–2013, 2013–2016, and 2016–2019), paralleling the 20-year analysis. Consistency between the two temporal scales was evaluated to assess sensitivity to monitoring duration. Results for RRAC and RROW are presented in Supplementary Figs. 7 and 8, respectively.

Spatial settings

For grid-cell total wetland area thresholds, we applied an alternative cutoff of 0.1 km^2. This threshold preserves over 99% of global tidal wetland area while excluding more than 20% of grid cells (Supplementary Table 1). The corresponding results, compared with those in Fig. 2, are shown in Supplementary Fig. 18.

For grid-cell resolution, we refined the analysis to 0.125° for area aggregation to compare the original 0.25° selection. The RSL change rates were resampled to 0.125° by uniformly assigning the original 0.25° values and uncertainties to the enclosed finer-scale cells. In addition, we used an independent RSL change rate reconstruction, for which the ASL trend was derived from the native 0.125° Copernicus Marine Service product, to examine its relationship with RRAC. The comparison between the two approaches is presented in Supplementary Fig. 19.

Individual datasets

For each individual area-change dataset, we performed a binned loss-gain analysis based on the corresponding RSL change rates, excluding uncertainties associated with total extent estimates and no-change classification. This approach isolates the sign of wetland area change in response to increasing RSL change rate, offering an alternative perspective (Supplementary Fig. 10). Additionally, we calculated RRAC magnitudes against RSL change rates for individual datasets to assess consistency across different area-change products, with results shown in Supplementary Fig. 17.

Data availability

All datasets used in this study are publicly available. Global local sea-level trends and associated uncertainties are available as a single netCDF file from SEANOE https://www.seanoe.org/data/00637/74862 (ref. 36). The vertical land motion dataset (including the present-day trends and associated uncertainties) is derived from https://zenodo.org/records/8308347 (ref. 37). Global salt marsh gain and loss maps from Campbell et al. are available from https://www.earthdata.nasa.gov/data/catalog/ornl-cloud-global-salt-marsh-change-2122-1 (ref. 34). Global mangrove change data developed by Bunting et al.[35] are available at https://zenodo.org/records/6894273. Another global tidal wetland (including marshes and mangroves) change dataset is accessible via Google Earth Engine platform from https://developers.google.com/earth-engine/datasets/catalog/JCU_Murray_GIC_global_tidal_wetland_change_2019 (ref. 3). Global tidal marsh extent is available at https://zenodo.org/records/8420753 (ref. 88) and mangrove extent is available at https://zenodo.org/records/12756047 (ref. 87). Global surface water distribution in 2020 is available via Google Earth Engine https://developers.google.com/earthengine/datasets/catalog/JRC_GSW1_4_YearlyHistory (ref. 90). The global aquaculture pond dataset is available at Zenodo https://doi.org/10.5281/zenodo.5643036 (ref. 91). Global distribution of tidal elevations, based on the FES2014 tides model, is accessed from AVISO https://www.aviso.altimetry.fr/en/data/products/auxiliary-products/global-tide-fes.html (ref. 93). Monthly averaged non-organic Solid Particulate Matter in sea water in netCDF format are available from Copernicus Global Ocean Colour at https://data.marine.copernicus.eu/product/OCEANCOLOUR_GLO_BGC_L4_NRT_009_102 (ref. 94). Tide gauge relative sea level trends are from NOAA https://tidesandcurrents.noaa.gov/sltrends/sltrends.html. Global ocean gridded sea surface heights of 0.125° resolution are available from Copernicus Marine Service at https://data.marine.copernicus.eu/product/SEALEVEL_GLO_PHY_L4_MY_008_047/services. Detailed processed data generated in this study are provided in the Zenodo repository at https://doi.org/10.5281/zenodo.18418452. Source data for the main figures are provided with this paper.

Code availability

Python scripts developed for this study, including code for data retrieval and processing, association analyses, and figure generation, are available in the Zenodo repository at https://doi.org/10.5281/zenodo.18418452.

References

1. Donato, D. C. et al. Mangroves among the most carbon-rich forests in the tropics. *Nat. Geosci.* **4**, 293–297 (2011).
2. Day, J. et al. Coastal wetlands in the Anthropocene. *Annu. Rev. Environ. Resour.* **49**, 105–135 (2024).
3. Murray, N. J. et al. High-resolution mapping of losses and gains of Earth's tidal wetlands. *Science* **376**, 744–749 (2022).
4. Schuerch, M. et al. Future response of global coastal wetlands to sea-level rise. *Nature* **561**, 231–234 (2018).
5. Kirwan, M. L. & Megonigal, J. P. Tidal wetland stability in the face of human impacts and sea-level rise. *Nature* **504**, 53–60 (2013).
6. Törnqvist, T. E., Jankowski, K. L., Li, Y.-X. & González, J. L. Tipping points of Mississippi Delta marshes due to accelerated sea-level rise. *Sci. Adv.* **6**, eaaz5512 (2020).

7. Hijma, M. P. et al. Global sea-level rise in the early Holocene revealed from North Sea peats. *Nature* **639**, 652–657 (2025).
8. Friess, D. A., Adame, M. F., Adams, J. B. & Lovelock, C. E. Mangrove forests under climate change in a 2 °C world. *WIREs Clim. Change* **13**, e792 (2022).
9. FitzGerald, D. M. & Hughes, Z. Marsh processes and their response to climate change and sea-level rise. *Annu. Rev. Earth Planet. Sci.* **47**, 481–517 (2019).
10. Rogers, K. et al. Wetland carbon storage controlled by millennial-scale variation in relative sea-level rise. *Nature* **567**, 91–95 (2019).
11. Saintilan, N. et al. Thresholds of mangrove survival under rapid sea level rise. *Science* **368**, 1118–1121 (2020).
12. Webb, E. L. et al. A global standard for monitoring coastal wetland vulnerability to accelerated sea-level rise. *Nat. Clim. Change* **3**, 458–465 (2013).
13. Woodroffe, C. D. et al. Mangrove sedimentation and response to relative sea-level rise. *Annu. Rev. Mar. Sci.* **8**, 243–266 (2016).
14. Saintilan, N. et al. Constraints on the adjustment of tidal marshes to accelerating sea level rise. *Science* **377**, 523–527 (2022).
15. Jankowski, K. L., Törnqvist, T. E. & Fernandes, A. M. Vulnerability of Louisiana's coastal wetlands to present-day rates of relative sea-level rise. *Nat. Commun.* **8**, 14792 (2017).
16. Li, G., Törnqvist, T. E. & Dangendorf, S. Real-world time-travel experiment shows ecosystem collapse due to anthropogenic climate change. *Nat. Commun.* **15**, 1226 (2024).
17. Lovelock, C. E. et al. The vulnerability of Indo-Pacific mangrove forests to sea-level rise. *Nature* **526**, 559–563 (2015).
18. Kirwan, M. L., Temmerman, S., Skeehan, E. E., Guntenspergen, G. R. & Fagherazzi, S. Overestimation of marsh vulnerability to sea level rise. *Nat. Clim. Change* **6**, 253–260 (2016).
19. Sadler, P. M. & Jerolmack, D. J. Scaling laws for aggradation, denudation and progradation rates: the case for time-scale invariance at sediment sources and sinks. *Geol. Soc. Lond. Spec. Publ.* **404**, 69–88 (2015).
20. Saintilan, N. et al. Widespread retreat of coastal habitat is likely at warming levels above 1.5 °C. *Nature* **621**, 112–119 (2023).
21. Morris, J. T., Sundareshwar, P. V., Nietch, C. T., Kjerfve, B. & Cahoon, D. R. Responses of coastal wetlands to rising sea level. *Ecology* **83**, 2869–2877 (2002).
22. Kirwan, M. L. & Mudd, S. M. Response of salt-marsh carbon accumulation to climate change. *Nature* **489**, 550–553 (2012).
23. Morris, J. T. et al. Mangrove trees outperform saltmarsh grasses in building elevation but collapse rapidly under high rates of sea-level rise. *Earth's. Future* **11**, e2022EF003202 (2023).
24. McKee, K. L., Cahoon, D. R. & Feller, I. C. Caribbean mangroves adjust to rising sea level through biotic controls on change in soil elevation. *Glob. Ecol. Biogeogr.* **16**, 545–556 (2007).
25. Sasmito, S. D., Murdiyarso, D., Friess, D. A. & Kurnianto, S. Can mangroves keep pace with contemporary sea level rise? A global data review. *Wetl. Ecol. Manag.* **24**, 263–278 (2016).
26. Morris, J. T. et al. Contributions of organic and inorganic matter to sediment volume and accretion in tidal wetlands at steady state. *Earth's. Future* **4**, 110–121 (2016).
27. Kirwan, M. L., Walters, D. C., Reay, W. G. & Carr, J. A. Sea level driven marsh expansion in a coupled model of marsh erosion and migration. *Geophys. Res. Lett.* **43**, 4366–4373 (2016).
28. Spencer, T. et al. Global coastal wetland change under sea-level rise and related stresses: the DIVA Wetland Change Model. *Glob. Planet. Change* **139**, 15–30 (2016).
29. Payo, A. et al. Projected changes in area of the Sundarban mangrove forest in Bangladesh due to SLR by 2100. *Clim. Change* **139**, 279–291 (2016).
30. Thorne, K. et al. U.S. Pacific coastal wetland resilience and vulnerability to sea-level rise. *Sci. Adv.* **4**, eaao3270 (2018).
31. Schuerch, M. et al. Large-scale loss of Mediterranean coastal marshes under rising sea levels by 2100. *Commun. Earth Environ.* **6**, 128 (2025).
32. Coleman, D. J. et al. Reconciling models and measurements of marsh vulnerability to sea level rise. *Limnol. Oceanogr. Lett.* **7**, 140–149 (2022).
33. Fagherazzi, S. et al. Salt marsh dynamics in a period of accelerated sea level rise. *JGR Earth Surf.* **125**, e2019JF005200 (2020).
34. Campbell, A. D., Fatoyinbo, L., Goldberg, L. & Lagomasino, D. Global hotspots of salt marsh change and carbon emissions. *Nature* **612**, 701–706 (2022).
35. Bunting, P. et al. Global mangrove extent change 1996–2020: Global Mangrove Watch version 3.0. *Remote Sens.* **14**, 3657 (2022).
36. Prandi, P. et al. Local sea level trends, accelerations and uncertainties over 1993–2019. *Sci. Data* **8**, 1 (2021).
37. Oelsmann, J. et al. Regional variations in relative sea-level changes influenced by nonlinear vertical land motion. *Nat. Geosci.* **17**, 137–144 (2024).
38. Hagger, V. et al. Drivers of global mangrove loss and gain in social-ecological systems. *Nat. Commun.* **13**, 6373 (2022).
39. Zhang, Z., Luo, X., Friess, D. A. & Li, Y. Global mangrove growth variability driven by climatic oscillation-induced sea-level fluctuations. *Nat. Geosci.* **18**, 488–494 (2025)
40. Lagomasino, D. et al. Storm surge and ponding explain mangrove dieback in southwest Florida following Hurricane Irma. *Nat. Commun.* **12**, 4003 (2021).
41. Goldberg, L., Lagomasino, D., Thomas, N. & Fatoyinbo, T. Global declines in human-driven mangrove loss. *Glob. Change Biol.* **26**, 5844–5855 (2020).
42. Mastrandrea, M. D. et al. *Guidance Note for Lead Authors of the IPCC Fifth Assessment Report on Consistent Treatment of Uncertainties* (Intergovernmental Panel on Climate Change, 2010).
43. Liang, X. et al. Hurricanes induced irreversible large-scale loss of mangrove forests. *Geophys. Res. Lett.* **52**, e2025GL115692 (2025).
44. Cahoon, D. R., Lynch, J. C., Roman, C. T., Schmit, J. P. & Skidds, D. E. Evaluating the relationship among wetland vertical development, elevation capital, sea-level rise and tidal marsh sustainability. *Estuaries Coasts* **42**, 1–15 (2019).
45. Barksdale, M. B., Valentine, K., Hein, C. J. & Kirwan, M. L. Tradeoffs between vertical and lateral resilience in a salt marsh restoration model. *J. Geophys. Res. Biogeosci.* **130**, e2025JG009145 (2025).
46. Morris, J. T. & Sundberg, K. Responses of coastal wetlands to rising sea-level revisited: the importance of organic production. *Estuaries Coast* **47**, 1735–1749 (2024).
47. Nienhuis, J. H. et al. Global-scale human impact on delta morphology has led to net land area gain. *Nature* **577**, 514–518 (2020).
48. Hou, X., Xie, D., Feng, L., Shen, F. & Nienhuis, J. H. Sustained increase in suspended sediments near global river deltas over the past two decades. *Nat. Commun.* **15**, 3319 (2024).
49. Dai, Z., Long, C., Mei, X., Fagherazzi, S. & Xiong, Y. Overestimation of mangroves deterioration from sea level rise in tropical deltas. *Geophys. Res. Lett.* **51**, e2024GL109675 (2024).
50. Xiong, Y. et al. Monsoon-driven waves induce a prevailing recession in mangrove forests across the Ganges–Brahmaputra–Meghna Delta. *Commun. Earth Environ.* **7**, 417 (2026).
51. Lou, Y., Dai, Z., Mei, X., Shi, H., Dong, H. & Cheng, J. Seaward expansion of salt marshes on the largest uninhabited island in Changjiang Estuary over the past two decades. *Ecol. Indic.* **178**, 114052 (2025).
52. Alongi, D. M. The impact of climate change on mangrove forests. *Curr. Clim. Change Rep.* **1**, 30–39 (2015).
53. Kirwan, M. L. & Gedan, K. B. Sea-level driven land conversion and the formation of ghost forests. *Nat. Clim. Change* **9**, 450–457 (2019).

54. Osland, M. J. et al. Migration and transformation of coastal wetlands in response to rising seas. *Sci. Adv.* **8**, eabo5174 (2022).
55. Hopkinson, C. S., Morris, J. T., Fagherazzi, S., Wollheim, W. M. & Raymond, P. A. Lateral marsh edge erosion as a source of sediments for vertical marsh accretion. *J. Geophys. Res. Biogeosci.* **123**, 2444–2465 (2018).
56. Mariotti, G. & Carr, J. Dual role of salt marsh retreat: long-term loss and short-term resilience. *Water Resour. Res.* **50**, 2963–2974 (2014).
57. FAO. *The World's Mangroves 2000–2020* (FAO, 2023).
58. Mu, D., Huang, R., Yin, P., Yan, H. & Xu, T. Reconstructing sea level rise from global 945 tide gauges since 1900. *Earth Syst. Sci. Data* **17**, 5507–5528 (2025).
59. Kemp, A. C. et al. Climate related sea-level variations over the past two millennia. *Proc. Natl. Acad. Sci. USA* **108**, 11017–11022 (2011).
60. Törnqvist, T. E., Cahoon, D. R., Morris, J. T. & Day, J. W. Coastal wetland resilience, accelerated sea-level rise, and the importance of timescale. *AGU Adv.* **2**, e2020AV000334 (2021).
61. IPCC. *Climate Change 2022: Impacts, Adaptation and Vulnerability* (eds Pörtner, H.-O. et al.) (Cambridge University Press, 2022).
62. IPCC. *Climate Change 2021: The Physical Science Basis* (eds Masson-Delmotte, V. et al.) (Cambridge University Press, 2021).
63. Ohenhen, L. O. et al. Global subsidence of river deltas. *Nature* **649**, 894–901 (2026).
64. Schwarz, C., Van Rees, F., Xie, D., Kleinhans, M. G. & Van Maanen, B. Salt marshes create more extensive channel networks than mangroves. *Nat. Commun.* **13**, 2017 (2022).
65. Saintilan, N., Wilson, N. C., Rogers, K., Rajkaran, A. & Krauss, K. W. Mangrove expansion and salt marsh decline at mangrove poleward limits. *Glob. Change Biol.* **20**, 147–157 (2014).
66. Cavanaugh, K. C. et al. Climate-driven regime shifts in a mangrove–salt marsh ecotone over the past 250 years. *Proc. Natl. Acad. Sci. USA* **116**, 21602–21608 (2019).
67. Leal, M. & Spalding, M. D. *The State of the World's Mangroves 2024* (Global Mangrove Alliance, 2024).
68. Kirwan, M. L. et al. Limits on the adaptability of coastal marshes to rising sea level. *Geophys. Res. Lett.* **37**, 2010GL045489 (2010).
69. Balke, T., Stock, M., Jensen, K., Bouma, T. J. & Kleyer, M. A global analysis of the seaward salt marsh extent: the importance of tidal range. *Water Resour. Res.* **52**, 3775–3786 (2016).
70. Holmquist, J. R., Brown, L. N. & MacDonald, G. M. Localized scenarios and latitudinal patterns of vertical and lateral resilience of tidal marshes to sea-level rise in the contiguous United States. *Earth's. Future* **9**, e2020EF001804 (2021).
71. Horstman, E. M., Dohmen-Janssen, C. M., Bouma, T. J. & Hulscher, S. J. M. H. Tidal-scale flow routing and sedimentation in mangrove forests: combining field data and numerical modelling. *Geomorphology* **228**, 244–262 (2015).
72. Ladd, C. J., Duggan-Edwards, M. F., Bouma, T. J., Pagès, J. F. & Skov, M. W. Sediment supply explains long-term and large-scale patterns in salt marsh lateral expansion and erosion. *Geophys. Res. Lett.* **46**, 11178–11187 (2019).
73. Xie, D., Schwarz, C., Kleinhans, M. G. et al. Mangrove removal exacerbates estuarine infilling through landscape-scale bio-morphodynamic feedbacks. *Nat. Commun.* **14**, 7310 (2023).
74. Zhang, X. et al. Quantifying expansion and removal of Spartina alterniflora on Chongming Island, China, using time series Landsat images during 1995–2018. *Remote Sens. Environ.* **247**, 111916 (2020).
75. Ellison, J. C. Impacts of sediment burial on mangroves. *Mar. Pollut. Bull.* **37**, 420–426 (1999).
76. Sidik, F., Neil, D. & Lovelock, C. E. Effect of high sedimentation rates on surface sediment dynamics and mangrove growth in the Porong River, Indonesia. *Mar. Pollut. Bull.* **107**, 355–363 (2016).
77. Nardin, W., Vona, I. & Fagherazzi, S. Sediment deposition affects mangrove forests in the Mekong delta, Vietnam. *Cont. Shelf Res.* **213**, 104319 (2021).
78. Ganju, N. K. et al. Sediment transport-based metrics of wetland stability. *Geophys. Res. Lett.* **42**, 7992–8000 (2015).
79. Langston, A. K., Alexander, C. R., Alber, M. & Kirwan, M. L. Beyond 2100: elevation capital disguises salt marsh vulnerability to sea-level rise in Georgia, USA. *Estuar. Coast. Shelf Sci.* **249**, 107093 (2021).
80. Kleinherenbrink, M., Riva, R. & Frederikse, T. A comparison of methods to estimate vertical land motion trends from GNSS and altimetry at tide gauge stations. *Ocean Sci.* **14**, 187–204 (2018).
81. Hamlington, B. D. et al. The rate of global sea level rise doubled during the past three decades. *Commun. Earth Environ.* **5**, 601 (2024).
82. Horton, B. P. et al. Predicting marsh vulnerability to sea-level rise using Holocene relative sea-level data. *Nat. Commun.* **9**, 2687 (2018).
83. Keogh, M. E. & Törnqvist, T. E. Measuring rates of present-day relative sea-level rise in low-elevation coastal zones: a critical evaluation. *Ocean Sci.* **15**, 61–73 (2019).
84. Oelsmann, J. et al. Subsidence more than doubles sea-level rise today along densely populated coasts. *Nat. Commun.* **17**, 4382 (2026).
85. Chen, Y. & Kirwan, M. L. Climate-driven decoupling of wetland and upland biomass trends on the mid-Atlantic coast. *Nat. Geosci.* **15**, 913–918 (2022).
86. Raabe, E. A. & Stumpf, R. P. Expansion of tidal marsh in response to sea-level rise: Gulf Coast of Florida, USA. *Estuaries Coast* **39**, 145–157 (2016).
87. Bunting, P. et al. Global mangrove watch: annual mangrove extent (Version 4.0.19) [Dataset]. Zenodo. Available at: https://doi.org/10.5281/zenodo.12756047 (2024).
88. Worthington, T. A. et al. The distribution of global tidal marshes from Earth observation data. *Glob. Ecol. Biogeogr.* **33**, e13852 (2024).
89. Xu, K., Wang, X., Jiang, C. & Sun, O. J. Assessing the vulnerability of ecosystems to climate change based on climate exposure, vegetation stability and productivity. *For. Ecosyst.* **7**, 23 (2020).
90. Pekel, J.-F., Cottam, A., Gorelick, N. & Belward, A. S. High-resolution mapping of global surface water and its long-term changes. *Nature* **540**, 418–422 (2016).
91. Wang, Z. et al. Global mapping of the landside clustering of aquaculture ponds from dense time-series 10 m Sentinel-2 images on Google Earth Engine. *Int. J. Appl. Earth Obs. Geoinf.* **115**, 103100 (2022).
92. Huber, P. J. Robust statistics. in (ed. Lovric, M.) *International Encyclopedia of Statistical Science*, 1248–1251 (Springer, 2011).
93. Lyard, F. H., Allain, D. J., Cancet, M., Carrère, L. & Picot, N. FES2014 global ocean tide atlas: design and performance. *Ocean Sci.* **17**, 615–649 (2021).
94. ACRI-ST. Copernicus Global Ocean Colour: Bio-Geo-Chemical, L4, from Satellite Observations (SPM) [Dataset] https://data.marine.copernicus.eu/product/OCEANCOLOUR_GLO_BGC_L4_MY_009_104/description (Copernicus Marine Service, 2021).
95. Liu, S. et al. Dynamics and drivers of tidal flat morphology in China. *Nat. Commun.* **16**, 2153 (2025).
96. O'brien, R. M. A caution regarding rules of thumb for variance inflation factors. *Qual. Quant.* **41**, 673–690 (2007).
97. Wu, W., Biber, P. & Bethel, M. Thresholds of sea-level rise rate and sea-level rise acceleration rate in a vulnerable coastal wetland. *Ecol. Evol.* **7**, 10890–10903 (2017).
98. Wu, W. Accounting for spatial patterns in deriving sea-level rise thresholds for salt marsh stability: more than just total areas? *Ecol. Indic.* **103**, 260–271 (2019).

Author contributions

Z.J.D., J.H.N., and J.J.L. conceptualized and designed the study. A.H. conducted data preprocessing and preliminary analyses. J.J.L. and J.H.N. collected and processed additional datasets. W.N., J.H.N., and J.W. contributed to refining the methodology. J.J.L., J.H.N., and Z.J.D. performed the data analysis. J.J.L., Z.J.D., and J.H.N. prepared the figures and tables and wrote the original draft. Z.J.D, J.H.N., W.N., and X.F.M. provided detailed feedback in subsequent revisions. Z.J.D. additionally provided funding support and supervised the work of the first author (J.J.L.). All authors (J.J.L., A.H., Z.J.D., W.N., X.F.M., J.W., and J.H.N.) contributed to editing and improving the manuscript.

Funding

This study was financially supported by the National Natural Science Key Foundation of China [42430406], National Key R&D Program of China [2023YFE0121200], the Shanghai International Science and Technology Cooperation Fund Project [23230713800] and the Funds for Ministry of Science and Technology of China (SKLEC).

Competing interests

The authors declare no competing interests.

Additional information

Supplementary information The online version contains Supplementary material available at https://doi.org/10.1038/s41467-026-76031-3.

Correspondence and requests for materials should be addressed to Zhijun Dai or Jaap H. Nienhuis.

Peer review information *Nature Communications* thanks Erik Horstman, Matthew Kirwan and Zhen Zhang for their contribution to the peer review of this work. A peer review file is available.